Alloy Reorganization and Dynamics in Group-10-Metal–Gallium Nanoparticles under Reactive Atmospheres: Impact on Local Environment and Reactivity

Quentin Pessemesse, Alexandre Pérochon, Christophe Copéret, Marie-Ève L Perrin, Pierre-Adrien Payard

Alloy Reorganization and Dynamics in Group-10-metal-Gallium Nanoparticles under Reactive Atmospheres: Impact on Local Environment and Reactivity

Quentin Pessemesse,[1,2] Alexandre Perochon,[1] Christophe Copéret,[2] Marie-Eve L. Perrin,*[1] Pierre-Adrien Payard*[1,3]

[1] Universite Claude Bernard Lyon I, CNRS, CPE-Lyon, UMR 5246, ICBMS, 1 rue Victor Grignard, F-69622 Villeurbanne Cedex, France

[2] ETH Zurich, Department of Chemistry and Applied Biosciences, Vladimir-Prelog Weg 1-5/10, CH-8093 Zurich, Switzerland

[3] Dunia Innovations, Magnusstraße 11, 12489 Berlin, Germany

Ab initio Molecular Dynamics, Blue Moon Sampling, Group 10 Metals, Gallium, Nanoparticles, Catalysis

ABSTRACT: Bimetallic nanoparticles are catalysts for reactions as CO_x hydrogenation or propane dehydrogenation. Recently, gallium has been identified as a promoter which enables dispersion of transition metal sites, raising their activity and selectivity. However, quantitative information on alloying dynamics under reaction conditions are not readily available and a general computational method to access such information is lacking. Here, an *ab initio* molecular dynamics workflow with enhanced sampling methods is used to probe the alloying behavior of Ni-, Pd-, and Pt-Ga nanoparticles under operating conditions (T = 600°C) in presence of H_2 or CO. The three metals display different alloying behaviors with Ga: Ni forms a core surrounded by gallium, while Pd and Pt form different alloyed structures. Both H_2 and CO shift the alloying state to different extents. A set of three descriptors is then proposed to compare and quantify the alloying behavior of these catalyst models: (i) the position α^{min} of the most stable alloying state; (ii) the curvature η_α of the free energy at α^{min}, referred to as the alloying hardness; (iii) the skew κ_α of the free energy at α^{min}, which relates to its propensity to alloy or segregate. The cost of alloy reorganization, which correlates with alloy hardness, is a major part of the free energy barriers of propane dehydrogenation.

Seeing as the alloying behavior of a catalyst is a critical parameter that is overlooked in catalyst design, quantitative descriptors are a first step in designing alloys with set catalytic properties.

INTRODUCTION

Supported bimetallic nanoparticles are ubiquitous catalysts in industrial chemical processes as they typically show improved performances (activity, selectivity and/or stability) compared to monometallic systems. One prominent example is the Oleflex propane dehydrogenation (PDH) process, which relies on PtSn-based supported catalysts.[1,2,3] Compared to pure Pt, the presence of Sn as a promoter slows deactivation through coking and sintering,[4,5] and improves selectivity toward the desired propene product. Similarly, Pt-based PDH catalysts are improved by alternative promoters such as Ga,[6] which have been recently implemented in industrial settings.[7,8,9,10,11,12] NiGa and PdGa have also been studied as PDH catalysts: PdGa displays significantly lower activity and faster deactivation than PtGa ($k_d \sim 10^2$ *vs* 10^{-2} h^{-1}),[13] while NiGa also favors propane cracking yielding ethylene and methane in place of the desired propene and H_2 products.[14,15] Notably, the introduction of Ga to group 10 metals has also been shown to significantly influence and to switch their established selectivity of these elements, in other reactions like CO_2 hydrogenation: group 10 metals are established catalysts for the reverse water–gas shift reaction (Pt,[16,17] Pd[18]) and for CO_2 methanation (Ni[19]) in the absence of promoters, but become selective toward methanol formation in the presence of Ga.[20,21,22]

These different reactivity patterns cannot be readily understood without understanding the dynamic structure of these catalysts. The changes in activity, stability and selectivity of these active metals (Ni, Pd, Pt) upon the addition of promoters, in particular Ga, correlate with the formation of alloyed bimetallic nanoparticles evidenced by X-Ray adsorption spectroscopy.[22,21,23,24] Notably, the alloying state in these bimetallic catalysts can be probed using H_2 or CO chemisorption, where a reduced surface coverage is experimentally found when Ga is present. This is typically interpreted as a decrease in available transition metal sites on the surface due to metal dilution through alloying.[5,22] In addition, infrared spectroscopy under CO atmosphere indicates a lower number of bridging CO molecules in the presence of Ga, consistent with the formation of an alloy. These characterization data show that the transition-metal atoms are dispersed in a Ga matrix, resulting in the formation of isolated sites.

[H]owever, both the precise nature of the alloy and the chemical environment of the metal sites under reactive atmospheres remain unknown. Indeed, the alloying state determined by chemisorption experiments does not necessarily reflect the alloying state under reaction conditions (high temperature, pressure, and presence of reactants, products and intermediates). Probe molecules, reactants and reaction intermediates can induce a restructuration of the catalyst.[25,26,27] *In*

situ and *Operando* spectroscopic measurements have been performed to characterize the chemical environment of the active site under reaction conditions. The incorporation of Ga(0) in group-10-metal nanoparticles under both PDH and CO_2 hydrogenation to methanol conditions has been confirmed by X-ray absorption spectroscopy. [5,23,24,28] However, identifying the composition and specific structure under reactive environment around the metal sites from spectroscopy is not straightforward. To address this issue, *Operando* modelling,[29] that is modelling the structure of the catalyst under realistic conditions, could serve as a valuable tool both in exploratory studies, and as a pre-requisite to interpret experimental findings.

Computational approaches to understand heterogeneous bimetallic catalysts usually rely on infinite slab models using static periodic DFT calculations.[30,31] These models bias the distribution of surface sites, in particular by underestimating the proportion of defects, as well as excluding dynamic restructuring of the system, i.e. the nano-scale restructuration of the catalyst due to the interaction with the support and adsorbates under operating conditions.[32] These phenomena are particularly prominent in highly dynamic bimetallic nanoparticles (< 2 nm). A given alloying state consists of an ensemble of structures with a common extent of alloying (*vide infra*). Thus, molecular dynamics simulations on small nanoparticle models are well-suited to sample these ensembles, and intrinsically recover most entropy contributions, including configurational entropy.[33] In addition, nanoparticle models include edge & vertex sites as well as other defects that are often absent in slab models. In this context, molecular dynamics simulations using parametrized force fields have been successfully used to investigate segregation in nano-alloys,[34,35] but this approach remains ill-suited to the investigation of adsorbates and their surface reactivity.

In that context, the *ab initio* molecular dynamics (AIMD) approach is well-suited to investigate the link between the alloying behavior of bimetallic catalysts and their activity.[36] Due to the high computational cost of the method (tens of minutes of CPU time per fs of simulation), the sampling must be enhanced to explore relevant structures on a reasonable time scale. To alleviate this issue, enhanced sampling methods have been recently implemented to model Mn segregation within PtMn-based nanoparticles, which proved useful to understand the X-ray absorption signature of the catalyst.[37] Similarly, the alloying state of PdGa-based CO_2 dehydrogenation catalysts could be gathered from AIMD studies.[38] Regarding the PtGa-based catalysts, its high propylene selectivity in PDH was linked to the isolation of Pt sites that favor propylene desorption over deep dehydrogenation to coke,[39] but the dynamics of NiGa systems were never investigated. The coking pathway was correlated with partial dealloying of the catalyst, but the phenomenon was not quantified as the alloying state was not explicitly sampled. Although fruitful information could be gathered from these simulations, no periodic trends in over group 10 metals could be obtained. Only qualitative conclusions were drawn so far due to the convergence rate limitation of metadynamics as a sampling method and the inefficient sampling of the alloying state.

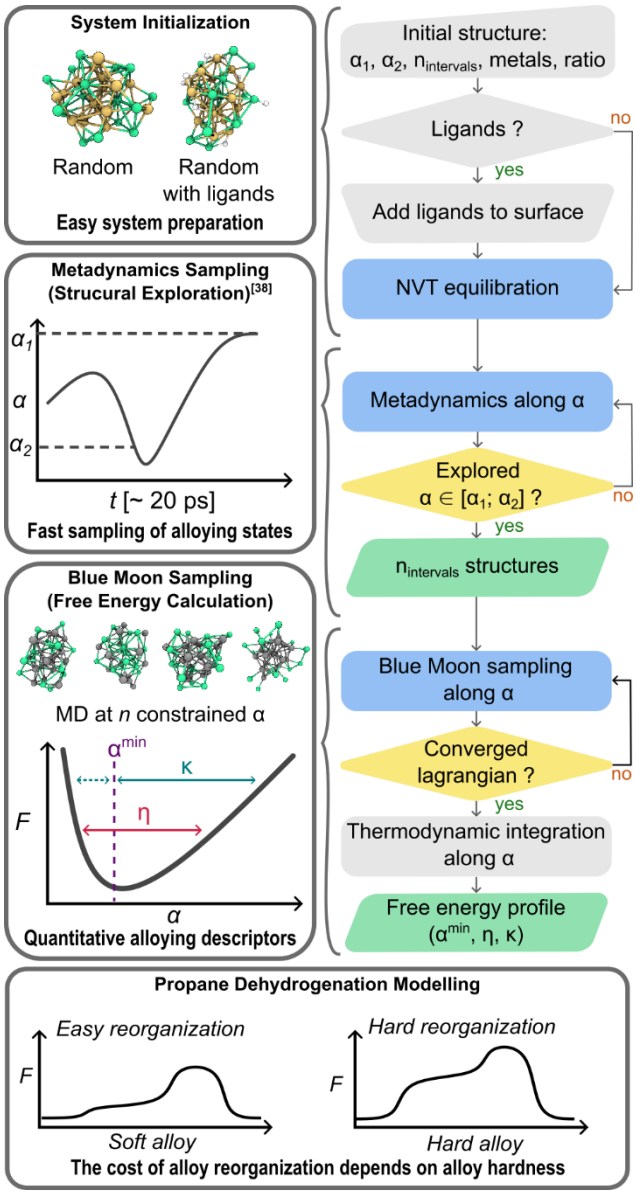

Figure 1. Computational workflow to model the alloying dynamics of nanoparticles.

These shortcomings can be traced back to the limitation of current computational methodologies that cannot be used to probe the influence of alloying on the structure and reactivity of bimetallic catalysts. Here, we develop a methodology to tackle this challenge (**Figure 1**); it consists first in a preliminary biased AIMD simulation (metadynamics[40]) using a single alloying parameter to ensure the exploration of representative structures for alloying states ranging from alternating to segregated alloys. Selected structures are then next used as starting points for free energy calculations (Blue Moon sampling[41]). This method provides quantitative insight into alloying-dealloying processes in nanometer-sized particles (36 atoms, *i.e.* ~ 1 nm), under relevant operating conditions of temperature (T = 600 °C) and adsorbate composition (vacuum, CO, H_2). In the case of Ni-, Pd-, and Pt-Ga systems, a set of quantitative statistical descriptors related to alloying was

extracted from AIMD simulations, unlocking simulations that quantify the influence of the alloying – dealloying process on the energy barriers of propane dehydrogenation.

COMPUTATIONAL DETAILS

$M_{18}Ga_{18}$ structures of approximately 1 nm in diameter were generated using Packmol.[42] While real catalysts have dispersity both in size and composition, this model was deemed sufficient to explore relevant alloying states and extract descriptors of catalytic activity. The structures were equilibrated using at least 2 ps of unbiased *ab initio* Molecular Dynamics (AIMD) in the NVT ensemble at the DFT level (see ESI section 1 for further computational details).

Metadynamics[40] simulations were run for 10 to 20 ps (see ESI section 2.1), starting from the equilibrated structures until structures with values of α at −0.5 and 0.5 were explored. The history-dependent bias consists of gaussian kernels with heights 0.01 Ha and width of 0.2, deposited along single collective variable, which was designed by taking inspiration from Cowley's short range order parameter α.[43] We define α as such (**Eq. 1**):

$$\alpha = 1 - 2\sum_{\mathrm{M}} \frac{CN(\mathrm{M}-\mathrm{Ga})}{CN(\mathrm{M}-\mathrm{Ga}) + CN(\mathrm{M}-\mathrm{M})} \quad (1)$$

where M = Ni, Pd, Pt and *CN*(X–Y) is defined as the following switch function based on interatomic distances (**Eq. 2**):

$$CN(X-Y) = \frac{1}{N_X}\sum_{i\in X}\sum_{i\in Y} \frac{1-\left(\frac{r_{ij}}{R_0}\right)^{NN}}{1-\left(\frac{r_{ij}}{R_0}\right)^{ND}} \quad (2)$$

where r_{ij} is the distance between atoms i and j, and R_0 is the critical length of the X–Y bond, taken to be 130% of the covalent radii, and NN and ND are empirical parameters defined as $ND = 2NN = 24$. The α collective variable represents the size of the interface between M and Ga. It is equivalent to a previously reported segregation parameter.[44] Three notable cases are: the alternating alloy: α = –1, the segregated structure: α = +1, and the entropic alloy: α = 0. While efficient exploration of the collective variable space is observed, this method suffers from slow convergence, making appropriate convergence out of reach given the computational cost of AIMD. Larger sets of collective variables led to much slower convergence, while multiple walkers metadynamics simulations led to unphysical behavior before convergence could be achieved. To solve the convergence issue of metadynamics, structures closest to the target values of alpha (-0.5, 0.4, ..., 0.5) were selected from metadynamics runs to carry out Blue Moon sampling of the free energy surface. Appropriate convergence of the Blue Moon sampling simulations was verified after 10 ps of simulation (see ESI figures S4–21). While this method is as computationally expensive as metadynamics, its fast convergence and ideal parallelization makes it a great match to extract quantitative information on 1 nm scale metallic nanoparticles. Given the importance of supported gallium-doped group-10-metal nanoparticles in catalysis, this workflow was used to probe the atomic structure of $Ni_{18}Ga_{18}$, $Pd_{18}Ga_{18}$ and $Pt_{18}Ga_{18}$ models.

Principal component regression of the free energy surface was used to interpret the results of the Blue Moon sampling simulations using the Scikit-Learn Python package. Simulations of propane dehydrogenation were carried out using metadynamics with a set of 4 collective variables: *CN*(C–H), *CN*(C–C), *CN*(M–H) and α (see ESI section 4). The definition in **Eq. 2** was used to define the coordination numbers, with R_0 also taken as the sum of the covalent radii. Gaussian kernels with height 0.001 Ha and width 0.2 were used for all the collective variables except α (width 0.1).

RESULTS AND DISCUSSION

Alloying and dynamics of Metal-Gallium nanoparticles. $Ni_{18}Ga_{18}$, $Pd_{18}Ga_{18}$ and $Pt_{18}Ga_{18}$ models were studied using the developed workflow which relies on metadynamics exploration followed by thermodynamic integration (*vide supra*). The sampling methods rely on a collective variable inspired by Cowley's short range order parameter *α* (**Eq. 1**),[43] which takes negative values for alloyed systems and positive ones for segregated ones. This workflow yields a free energy surface as a function of *α* for each system.

We consider three descriptors to capture the bimetallic nanoparticle's alloying behavior from the free energy surface along the alloying parameter α. First, the α^{min} value, which corresponds to the minimum of the free energy surface, can be referred to as the alloy position. It indicates the most stable alloying state. Next is the curvature (second derivative) η of the free energy at α^{min}, which refers to as the alloying hardness. It represents the energetic cost associated to a change in alloying state. The concept is in analogy with Pearson's and Parr's definition of chemical hardness where the second derivative of the energy with respect to the number of electrons captures the ease of deformation of the electron cloud or polarizability.[45] Last is the third derivative κ of the free energy at α^{min}, referred to as the alloy's skew. It indicates the difference in alloying hardness in either direction away from α^{min}; positive values indicate easier alloying, and negative values indicate easier segregation. These three descriptors are characteristic of a given alloying behavior (**Figure 1**). A gaussian process regression methodology is used to extract these descriptors from the sparse Blue Moon sampling free energy surface (see ESI section 3.2). At first glance, the three systems display different alloying behavior (**Figure 2.A** and **Figure 2.B**). The $Ni_{18}Ga_{18}$ model, with a single global free energy minimum obtained for $\alpha^{min} = 0.273$, is the least alloyed and corresponds to a core-shell-type structure (**Figure 2.B.1**). In contrast, $Pt_{18}Ga_{18}$ converges with $\alpha^{min} = -0.173$ and is thus the most homogenously alloyed system (**Figure 2.B.2**), while $Pd_{18}Ga_{18}$ with $\alpha^{min} = -0.127$ displays an intermediate behavior between Ni and Pt (**Figure 2.B.3**). The results for the PdGa and PtGa systems are in good agreement with experimental EXAFS data as well as with previous MD and MTD calculations performed on similar systems.[37,39] In addition, the unique core-shell structure of NiGa was not previously discussed, due to the larger nanoparticles size obtained in prepared catalysts.[21]

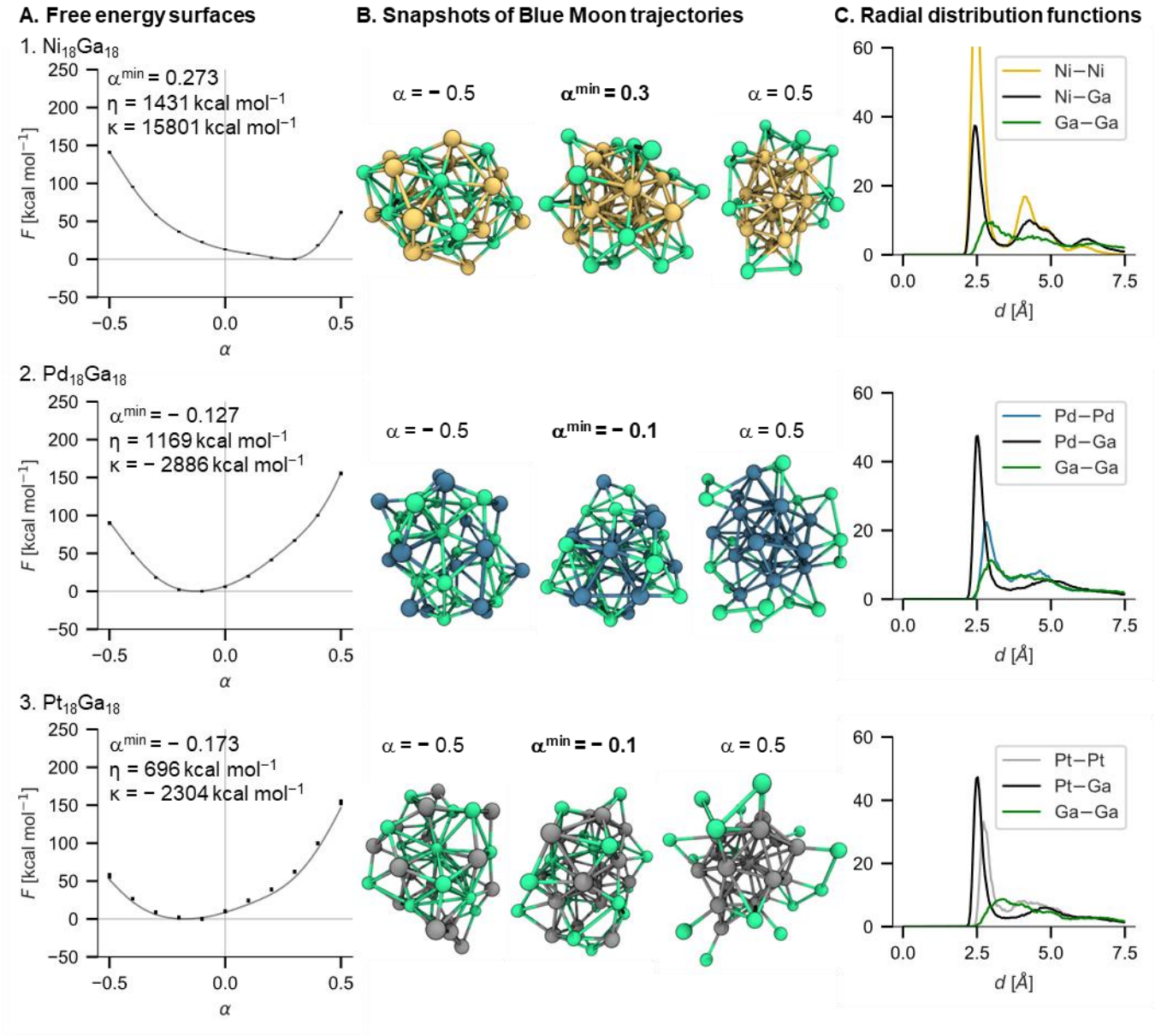

Figure 2. **A.** Free energy surfaces (black error bars) as obtained from thermodynamic integration in the Blue Moon ensemble, and the integrated gaussian process regression fit of the mean Lagrange multiplier (grey solid line). **B.** Snapshots of Blue Moon sampling trajectories for selected values of α. **C.** Radial distribution functions for the minimum free energy trajectory. Color coding: Ni – yellow; Pd – blue; Pt – grey; Ga – green.

Table 1 Values of alloy position(α^{min}), alloying hardness (η) and skew (κ) for each of $M_{18}Ga_{18}L_9$ model, L = none, H, CO; M = Ni, Pd, Pt. The values and standard errors are obtained by a gaussian process regression of the mean Lagrange multiplier, the R^2 of the fit is given for each model (see ESI section 3.2 for details on the fitting process).

	$Ni_{18}Ga_{18}L_9$	$Pd_{18}Ga_{18}L_9$	$Pt_{18}Ga_{18}L_9$

L	none	H_9	$(CO)_9$	none	H_9	$(CO)_9$	none	H_9	$(CO)_9$
R^2	0.9994	0.9984	0.9994	0.9994	0.9970	0.9970	0.9903	0.9987	0.9987
a^{min}	0.273 ± 0.005	0.152 ± 0.017	0.003 ± 0.008	− 0.127 ± 0.007	− 0.107 ± 0.006	−0.119 ± 0.006	− 0.173 ± 0.017	− 0.081 ± 0.012	− 0.064 ± 0.013
η [kcal mol^{-1}]	1431 ± 99	474 ± 73	754 ± 41	1169 ± 59	927 ± 54	766 ± 18	696 ± 75	745 ± 62	642 ± 28
κ [kcal mol^{-1}]	15801 ± 1440	2940 ± 1320	-2615 ± 1082	− 2886 ± 294	− 2068 ± 281	− 406 ± 95	− 2304 ± 730	− 2196 ± 486	−490 ± 240

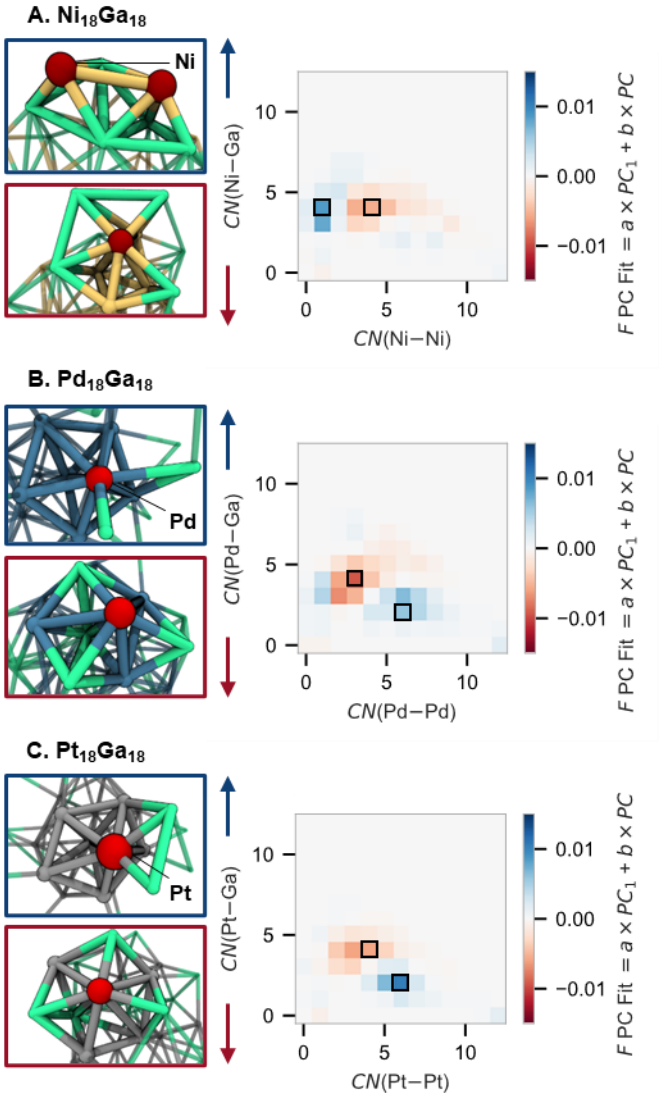

Figure 3. Coefficients of the principal component regression of the free energy surface, correlating to the free energy of individual coordination environments for the metal sites. Snapshots corresponding to typically favored (red box) and disfavored (blue box) metal sites (in red).

The three systems display variable free energy costs for alloying-segregation processes, as described by hardness η and skew κ parameters (**Figure 2** and **Table**). The hardness across the series increases as follows: $Pt_{18}Ga_{18}$ (η_{PtGa} = 696 kcal mol^{-1}) < $Pd_{18}Ga_{18}$ (η_{PdGa} = 1169 kcal mol^{-1}) < $Ni_{18}Ga_{18}$ (η_{NiGa} = 1431 kcal mol^{-1}). The skew κ is positive for $Ni_{18}Ga_{18}$,indicating that further alloying is more favorable than dealloying, while the smaller and negative skew of $Pd_{18}Ga_{18}$ and $Pt_{18}Ga_{18}$ indicates a preference for dealloying of the heavier two metals (κ_{NiGa} = 15'801 kcal mol^{-1} > κ_{PdGa} = − 2886 kcal mol^{-1} ~ κ_{PtGa} = − 2304 kcal mol^{-1}). Down the group 10 column, $M_{18}Ga_{18}$ nanoparticles become more alloyed, softer, and less skewed toward alloying (lower α^{min}, η and κ as reported in **Table**).

Alloying Analyses. The important changes in alloying behaviors of bimetallic nanoparticles relate to the varying stability of different metal atoms in given coordination environments. A principal component regression (PCR) methodology was used to identify the discrete sites that are responsible for a given alloying state. The free energy as a function of the alloying state $F(\alpha)$ was fitted with the first two principal components of the distribution of M–M and M–Ga coordination numbers along each constrained MD trajectory (See ESI section 4.1). The weighted coefficient of each type of site in the principal component fit for each type of noble metal site represents their correlation with the alloying free energy.

The alloying behaviors of Ni-, Pd- and Pt-based alloys can be traced back to ensembles of stable (negative coefficients) and unstable sites (positive coefficients). For $Ni_{18}Ga_{18}$, high-Ni-coordination spheres sites are relatively more stable than high-Ga ones (**Figure 3.A.1**; sites with negative coefficients are at or below the CN(M-Ga) = CN(M-M) diagonal). This favors the formation of a core-shell type structure. The distribution of coefficients for $Pd_{18}Ga_{18}$ is more symmetrical: both high Ga- and high-Pd coordination is disfavored, leading to an entropic alloy (**Figure 3.A.2**; sites with positive coefficients are away from the diagonal). $Pt_{18}Ga_{18}$ organizes in an alternating alloy due to the increased stability of sites with a high Ga coordination (**Figure 3.A.3**; sites with positive coefficients are at or above the diagonal). These quantitative descriptors point to which type of site is correlated to a stable alloying state.

The coefficients of the two components of the free energy surface fit provide additional information on the origin of this stability difference. The first component (a × PC1, ESI figures S22-24, a.d.) is linear with α, and takes opposite signs for high-M coordination spheres compared to high-Ga ones. This component seemingly captures the enthalpic component of alloying, with a difference in bonding energy between homometallic and heterometallic bonds. For the Ni-based alloy, the formation of homometallic bonds is energetically favored, while heterometallic bonds are energetically favored in Pt-based alloys. In the case of the Pd-based alloy, the first principal component has a negligible weight in the free energy surface fit: Pd-Ga and Pd-Pd bonds seem nearly isoenergetic in this case, and the alloy is entropically driven.

The second component of the fit (b × PC2, ESI figures S22-24 b. e.) takes more negative values for the entropically favored CN(M-M) ~ CN(M-Ga) ~ 5 environment, while high Ga or M coordination around M sites are disfavored. Thereof, PC2 captures the mixing entropy, as well as the disfavored Ga-Ga interaction, leading to a quadratic distribution skewed toward higher Ga environments for the three studied systems. While the entropic contribution in b × PC2 always favors alloying, the magnitude of the effect is not sufficient to overcome the enthalpic contribution in the case of $Ni_{18}Ga_{18}$. The two components of the fit capture energetic and entropic contributions to the free energy, which helps rationalize the behavior of the different metals in combination with gallium.

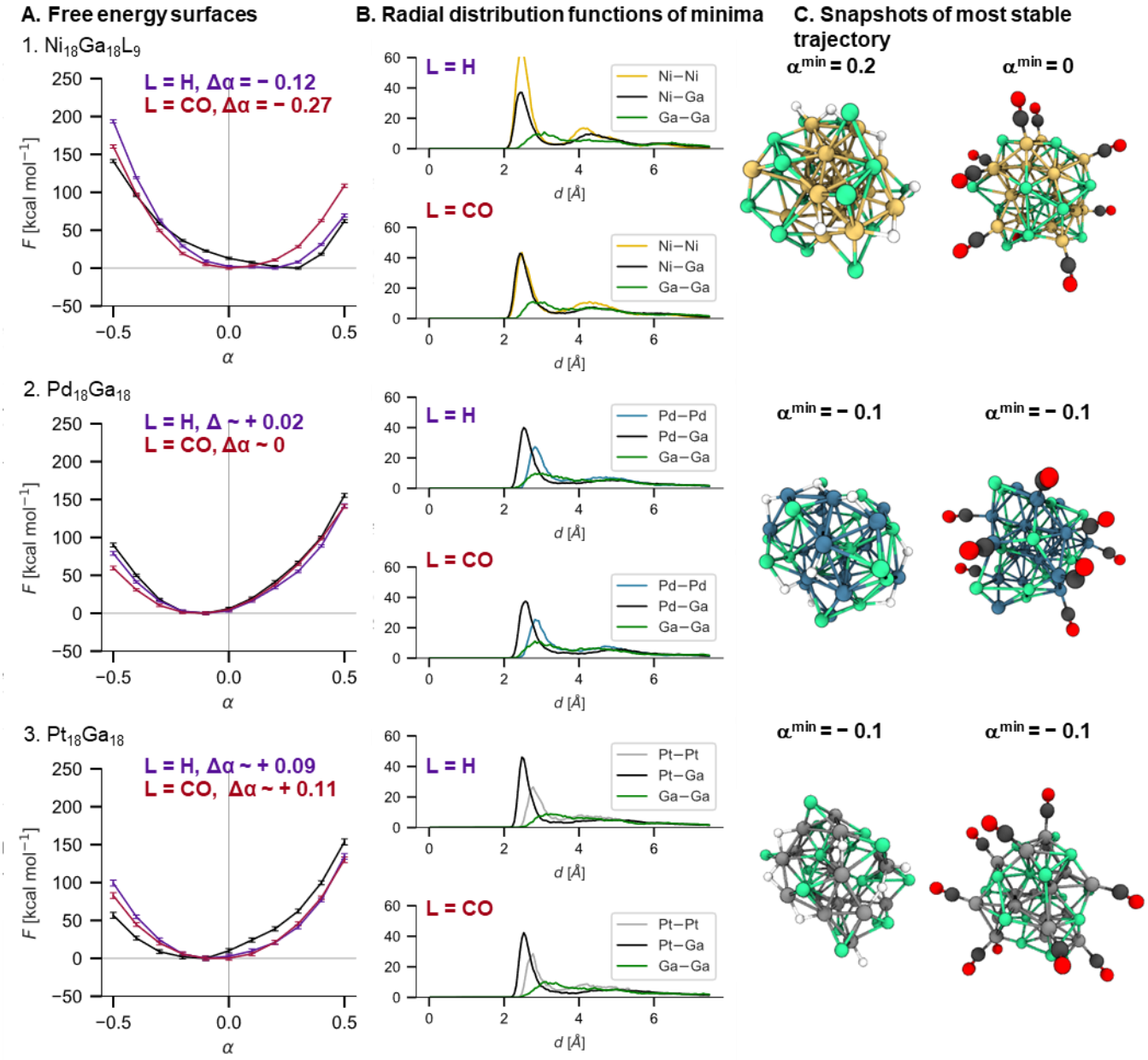

Figure 4. **A**. Free energy surfaces (error bars) as obtained from thermodynamic integration in the Blue Moon ensemble, and the integrated gaussian process regression fit of the mean Lagrange multiplier (solid line). **B**. Radial distributions. **C**. selected snapshots from the blue moon sampling trajectories for the $M_{18}Ga_{18}L_9$ (M = Ni, Pd, Pt; L = H, CO). Color coding: Ni – yellow; Pd – blue; Pt – grey; Ga – green, C – dark grey, O – red, H – white.

Effect of the gas phase composition on alloying state. The developed AIMD workflow herein developed is capable of predicting the alloying behavior of ligandless nanoparticles. However, under chemisorption or catalytic conditions, the adsorption of molecules on the catalyst can induce a reorganization of the catalyst's surface, thereby altering available surface/active sites. Therefore, we have expanded our study to include $M_{18}Ga_{18}L_9$ (M = Ni, Pt, Ga; L = CO, ½ H_2) as a proof of concept to demonstrate the capability of the designed workflow to describe catalyst restructuring under reactive

atmospheres. CO and H_2 are used as typical probe molecules for supported species, and display different properties with H being purely σ-donating while CO is π-accepting as well. They are also relevant in catalysis, as reactants or coproducts. Given the high exergonicity of H_2 dissociation at group 10 metals, adsorbed H_2 is modelled with its hydride form. The coverage was chosen to account to around half of the metal atoms being covered, which is consistent with experimental data for CO-covered PdGa.[46] The coverage in H was chosen equal to that of CO to facilitate comparison. Metadynamics simulation of the model clusters were carried out using the same parameters as in the ligandless case as depicted above, followed by thermodynamic integration in the blue moon ensemble.

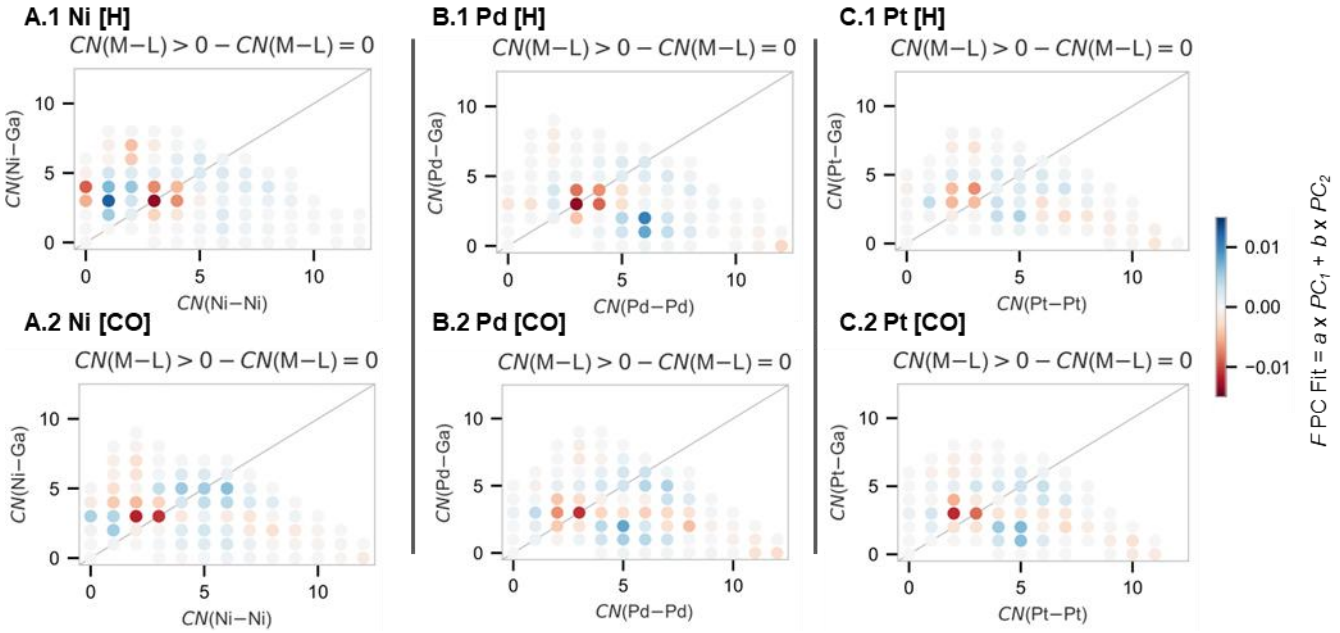

Figure 5. Difference in the coefficients for CN(M–L) > 0 and CN(M–L) = 0 of the principal component fits for $Ni_{18}Ga_{18}L_9$ (**A.**), $Pd_{18}Ga_{18}L_9$ (**B.**) and $Pt_{18}Ga_{18}L_9$ (**C.**), with L = H (**1**) and L = CO (**2**).

All the studied alloys undergo significant reorganization of the alloying state in the presence of ligands. $Ni_{18}Ga_{18}$ undergoes the most important shift in alloy position under the effect of ligands, with H and CO increasing alloying (α^{min}(H) ~ 0.1; α^{min}(CO) ~ 0, **Figure 4.A.1**), while the alloying hardness decreases. This translates into a stark modification of the radial distribution function: the second sphere of Ni becomes more disordered with increasing ligand field strength (**Figure 4.B.1**). This is consistent with migration of Ni from the bulk, to form islands of ligated Ni surrounded by mobile Ga atoms at the surface of the particle (**Figure 4.C.1**).

$Pd_{18}Ga_{18}$ is less affected by the presence of ligands than $Ni_{18}Ga_{18}$, with an almost insignificant increase of the alloy position with α^{min}(H) = − 0.107 and α^{min}(CO) = − 0.119. However, the dynamics of the alloying state above the minimum is affected, as a stronger field ligand skews the free energy surface toward lower a values: further alloying of Ga becomes more favorable (**Figure 4.A.2**). The alloying hardness decreases with ligand coordination, while the radial distribution function indicates a

more disordered second sphere. The reorganization of the first sphere of ligated atoms is responsible for the effect (**Figure 4.B.1**).

Both H and CO coordination to $Pt_{18}Ga_{18}$ cause a slight dealloying regardless of with $\alpha^{min}(H) = -0.081$ $\alpha^{min}(CO) = -0.064$, without modifying the hardness of the alloy (**Figure 4.A.3**). CO leads to an alloying state that is slightly more skewed toward alloying, while H does not alter the skew of the free energy surface. Both H and CO promote an alloying state close the entropic alloy at $\alpha = 0$.

Ligand coordination affects the three systems differently, usually leading to reduced alloy hardness and disordering of the second metal-metal coordination sphere. This "melting" of the nanoparticle upon ligand coordination leads to structures closer to the entropic alloy, highlighting the importance of the ligand coverage in determining the alloying behavior of the catalyst.

The coordination of ligands alters the alloying behavior of all three systems, due to the stabilization of certain surface sites. These sites could be identified using PCR of $F(\alpha)$ with the principal components of the distribution of coordination numbers around M (CN(M–M); CN(M–Ga); CN(M–L)). The weighted coefficients of the fit of $F(\alpha)$ indicate which ligandless and liganded sites are stabilizing. The difference between the coefficients for CN(M–L) > 0 and for CN(M–L) = 0 is negative for sites which are stabilized by ligands, and *vice versa* (**Figure 5**, ESI figures S25-36).

The tendency toward the formation of an entropic alloy can be rationalized using PCR of the distribution of coordination numbers of the group 10 metal. All the ligands seem to stabilize sites with 5, 6 and 7-coordinate sites with nearly equal shares of Ni and Ga in their coordination spheres (**Figure 5.A.2**). Consistent with radial distribution function analysis, this indicates a ligand-promoted "melting" of bimetallic nanoparticles upon ligand coordination. In the case of $Ni_{18}Ga_{18}H_8$, the prevalence of Ga-surrounded low-coordinate NiH sites at the surface of the particle is of relevance for (de-)hydrogenation catalysis. While ligand coordination less strongly affects the alloying behavior of Pd and Pt alloys, PCR indicates an important reorganization of the site distribution upon ligand coordination. Overall, these quantitative PCR descriptors enable the identification of key sites at the surface of the particle.

Alloying dynamics during propane dehydrogenation

As discussed above, the alloying behavior of Ga with group-10-metals differs significantly and is further influenced by the ligands adsorbed on the catalyst surface. This dynamic interaction affects the structure and could influence reaction mechanisms. The segregation of bimetallic alloys has been reported to either increase or decrease the catalytic activity of different bimetallic catalysts.[47,48] Here, propane dehydrogenation was chosen as a model reaction to study the role of alloying-segregation processes in reaction mechanisms, as previous computational studies suggest that structural changes

take place during reactions at the Pt_2Ga surface during the dehydrogenation of propylene to coke precursors.[49] Metadynamics simulations of propane dehydrogenation on $Ni_{18}Ga_{18}$ and $Pt_{18}Ga_{18}$ were conducted to delineate the influence of alloying-segregation processes on elementary steps on prototypes of soft and hard alloys (see computational details). The bias was applied on four collective variables: the C–H, C–M and C–C coordination numbers (*CN*), and the α alloying parameter. This set of collective variables enables the exploration of both adsorption and desorption processes (*CN*(C–M)), (de-)coordination (*CN*(M-H)), dehydrogenation (*CN*(C–H)), and alloying-dealloying processes (α). The metadynamics runs were stopped at the first desorption of propylene and the free-energy surfaces were obtained by reweighting of the probability distribution along α and *CN*(C–H). While only qualitative convergence of the metadynamics simulations is achievable at this level of theory, qualitative free energy barriers already clarify the role played by alloying-segregation processes in dehydrogenation mechanisms.

In the case of $Ni_{18}Ga_{18}$, the simulation reveals a fast dehydrogenation of propane to propene. The reaction starts with the C-H activation of the CH_2 moiety at an isolated Ni surface site. The resulting hydride is rapidly transferred to a neighboring Ni site, yielding an isopropylnickel surface site along with a bridging hydride that rapidly diffuses over the particle. C–H activation and alloy reorganization are sequential, and not concerted, as they take place on different time scales (~ 10 fs *vs.* ~ 1 ps). Thereof, the overall elementary step barrier for the C–H activation $\Delta F^{\ddagger}$ can be decomposed into contributions from the fast C–H bond cleavage $\Delta_{CH}F^{\ddagger}$ and from the slow alloy reorganization $\Delta_{\alpha}F^{\ddagger}$ (**Eq. 3**).

$$\Delta F^{\ddagger} = \Delta_{\alpha}F^{\ddagger} + \Delta_{CH}F^{\ddagger} \quad (3)$$

The alloying state evolves toward a more alloyed structure before the first C–H bond cleavage. The alloy reorganization contribution dominates the total free energy barrier ($\Delta_{CH}F^{\ddagger}$ = 13.1 kcal mol^{-1} *vs.* $\Delta_{\alpha}F^{\ddagger}$ = 17.2 kcal mol^{-1}, Error! Reference source not found.**A**). The high cost of alloy reorganization is consistent with NiGa being a hard alloy. The second C–H activation is the β-hydride elimination from one of the two methyl groups (yielding propene). Similarly to the first step, the cleavage is preceded by a further alloying of the particle, where core Ni atoms migrate into the Ga shell. The interaction of group 10 metals with Ga is known to increase their electron density.[50] A higher surface concentration in Ni will lead to a reduced electron density, which is known to favor agostic interactions and the subsequent β-hydride elimination in transition metal complexes.[51] Given the high alloy hardness of $Ni_{18}Ga_{18}$, alloying is endergonic and the reorganization contribution necessary to provide low electron density for the β-hydride elimination has a significant impact on the barrier ($\Delta_{\alpha}F^{\ddagger}$ = 11.8 kcal mol^{-1} *vs.* $\Delta_{CH}F^{\ddagger}$ = 20.0 kcal mol^{-1}). In this case, the concepts applicable to C–H activation and β-hydride in molecular metal complexes are transferable to the interpretation of reactivity at metal nanoparticles,[52] but alloying descriptors are necessary to fully understand the mechanism of C–H activation.

Propane dehydrogenation on $Pt_{18}Ga_{18}$ (Error! Reference source not found.**.B**) takes place via a similar mechanism: two subsequent C–H bonds activation at Pt single site to yield propene, but $Pt_{18}Ga_{18}$ features a different alloying behavior during the reaction compared to $Ni_{18}Ga_{18}$, as suggested by the alloying free energy surfaces (**Figure 2**). The first C–H activation, at the central carbon, is preceded by the segregation of Pt which contributes to the barrier ($\Delta_{\alpha}F^{\ddagger}$ = 12.4 kcal mol^{-1} *vs.* $\Delta_{CH}F^{\ddagger}$ = 14.7 kcal mol^{-1}). The alloy reorganization contribution for PtGa is less important than for NiGa, which is consistent with a softer alloying state for PtGa. After the first C–H activation the relaxation of the particle to a more alloyed state is mostly exergonic. The second C–H activation requires little reorganization after the initial relaxation, and thus the bond cleavage contribution dominates ($\Delta_{\alpha}F^{\ddagger}$ = 6.5 kcal mol^{-1} *vs.* $\Delta_{CH}F^{\ddagger}$ = 22.2 kcal mol^{-1}).

The crucial role played by alloying state dynamics in the mechanism of propane dehydrogenation was further demonstrated by carrying out metadynamics run with identical parameters, but with a constrained alloying state α. In both cases, the reaction follows different mechanisms where the terminal C–H bond is activated first, and the predicted energy barriers are affected (see ESI section 5.2). This shows that neglecting alloy reorganization does not enable a proper description of the system. The metadynamics simulations of propane dehydrogenation over $Ni_{18}Ga_{18}$ and $Pt_{18}Ga_{18}$ suggest that the two alloys behave differently. In $Ni_{18}Ga_{18}$, endergonic alloying is necessary prior to both bond cleavages, suggesting that reducing the electron density at Ni is important to favor bond activation. This reorganization represents a significant contribution to the free energy barrier (> 50 %). On the contrary, alloy reorganization in $Pt_{18}Ga_{18}$ has a non-negligible but much smaller impact on the overall free energy barrier (20-45%). The concept of alloying hardness and skew can help understand the reactivity of bimetallic nanoparticles: in hard alloys, the contribution of the alloy reorganization is higher than in soft alloys, while the sign of the skew helps to predict the direction of the alloying variations. These descriptors help us predict the higher contribution of alloy reorganization in C–H activation barriers in $Ni_{18}Ga_{18}$ compared to $Pt_{18}Ga_{18}$.

CONCLUSION

In the present study the structures of nanometer-sized clusters were explored using biased AIMD. Biasing the simulations ensures a reliable exploration of large-scale alloy reorganization, and the DFT level of theory makes this method more general than parametrized force fields. A set of descriptors, transferable to any alloy, was developed to compare alloying free energy surfaces: the alloy position (α^{min}), the alloying hardness (η) and the alloy's skew (κ).

The Ni-, Pd- and Pt-Ga models have different alloying states, going from hard, core-shell-type alloys (Ni-Ga) to softer alternating to entropic alloys (Pd-, Pt-Ga). Both CO and H_2 ligands alter the alloy position α, its hardness η as well as its skew κ. The alloying state of a given nanoparticle and the changes upon ligand coordination could be interpreted in terms of the

relative stability of discrete coordination environments for the group-10-metal, using a principal component analysis methodology.

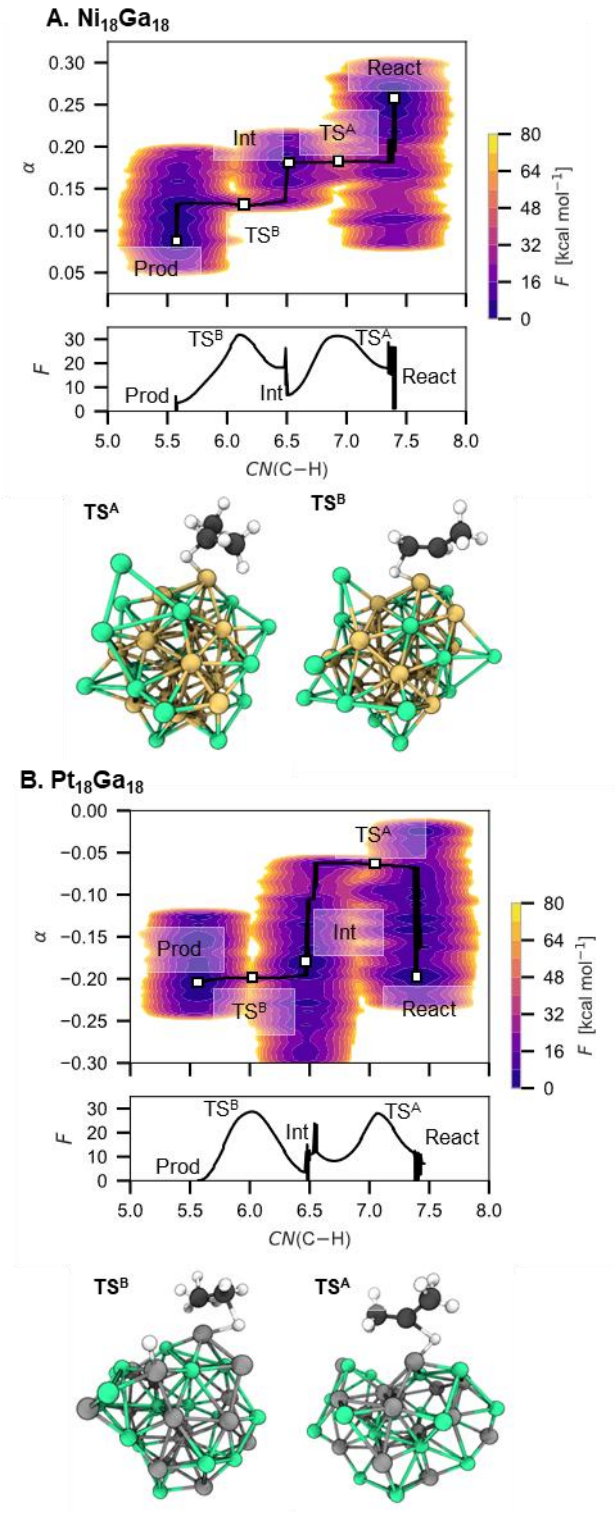

Figure 6. Free energy surface projected along CN(C–H) and α, and free energy profiles projected along each dimension, as obtained from metadynamics simulations and snapshots corresponding to the transition state for $Ni_{18}Ga_{18}$ (**A**) and $Pt_{18}Ga_{18}$ (**B**).

The alloying parameter α can be used as part of the reaction coordinate to explore the effect of the alloying state on the reactivity of a nanoparticle. In the case of propane dehydrogenation, the variations of α are a crucial part of the reaction coordinate. The different alloys accommodate the elementary steps in different manners, which can be predicted from the previously introduced descriptor set. While the necessary alloying of the hard Ni-Ga during the reaction is highly endergonic, alloying changes in Pt-Ga are much less prevalent. These results highlight the importance of taking alloy reorganization into account when modelling reaction mechanisms in heterogeneous catalysis. Alloying descriptors are also useful to quantify differences in the alloying behavior of different catalytic systems. They are also necessary to encourage the exploration of alloying states, or to monitor alloying changes during reactions. This workflow ought to be adapted to more realistic systems, that include but are not limited to explicit support-particle interactions, an important component across heterogeneous catalysts. We are convinced that investigating the evolution of the alloying state of complex catalytic systems under operating conditions will bring the deeper understanding required to rationalize the behavior of these catalysts, and to promote their computer-assisted design.

ASSOCIATED CONTENT

Additional figures.

Extended computational details.

Computational data are available free of charge at https://doi.org/10.5281/zenodo.14639627

This material is available free of charge via the Internet at http://pubs.acs.org.

AUTHOR INFORMATION

Corresponding Authors

marie-eve.perrin@univ-lyon1.fr

pa@dunia.ai

Funding Sources

This project was provided with computer and storage resources by GENCI at TGCC thanks to grant A0160813435 on the supercomputer Joliot Curie's ROME partition. *We gratefully acknowledge support from the PSMN (Pôle Scientifique de Modélisation Numérique) of the ENS de Lyon, and the Euler cluster of ETH Zurich, for computing resources. QP acknowledges funding by the French Ministry of Higher Education and Research (CDSN PhD grant).*

ACKNOWLEDGMENT

Dr C. Chizallet (IFPEN), Dr C. Raynaud (Univ Montpelier), Dr. E. Pidko (TU Delft), and Prof. O. Eisenstein (Univ Montpellier) are gratefully acknowledged for advice and fruitful discussions.

TOC

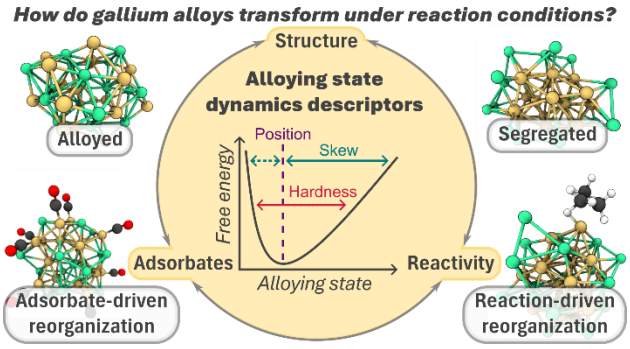

[1] Burch, R. Platinum-Tin Reforming Catalysts I. The Oxidation State of Tin and the Interaction between Platinum and Tin. J. Catal., **1981**, *71*, 348–359. https://doi.org/10.1016/0021-9517(81)90238-4.

[2] Bariås, O. A.; Holmen, A.; Blekkan, E. A. Propane Dehydrogenation over Supported Platinum Catalysts: Effect of Tin as a Promoter. *Catal. Today*, **1995**, *24*, 361–364. https://doi.org/10.1016/0920-5861(95)00059-o.

[3] Nawaz, Z. Light Alkane Dehydrogenation to Light Olefin Technologies: A Comprehensive Review. *Rev. Chem. Eng.*, **2015**, *31*. https://doi.org/10.1515/revce-2015-0012.

[4] Jablonski, E. L.; Castro, A. A.; Scelza, O. A.; de Miguel, S. R. Effect of Ga Addition to Pt/Al2O3 on the Activity, Selectivity and Deactivation in the Propane Dehydrogenation. *Appl. Catal. A: Gen.*, **1999**, *183*, 189–198. https://doi.org/10.1016/s0926-860x(99)00058-7.

[5] Searles, K.; Chan, K. W.; Mendes Burak, J. A.; Zemlyanov, D.; Safonova, O.; Copéret, C. Highly Productive Propane Dehydrogenation Catalyst Using Silica-Supported Ga–Pt Nanoparticles Generated from Single-Sites. *J. Am. Chem. Soc.*, **2018**, *140*, 11674–11679. https://doi.org/10.1021/jacs.8b05378.

[6] Sattler, J. J. H. B.; Gonzalez-Jimenez, I. D.; Luo, L.; Stears, B. A.; Malek, A.; Barton, D. G.; Kilos, B. A.; Kaminsky, M. P.; Verhoeven, T. W. G. M.; Koers, E. J.; Baldus, M.; Weckhuysen, B. M. Platinum-Promoted Ga/Al2O3 as Highly Active, Selective, and Stable Catalyst for the Dehydrogenation of Propane. *Angew. Chem. Int. Ed.*, **2014**, *53*, 9251–9256. https://doi.org/10.1002/anie.201404460.

[7] Pretz, M.; Fish, B.; Luo, L.; Stears, B. Shaping the future of on-purpose propylene production. *Hydrocarbon processing*, April 2017**.** https://www.hydrocarbonprocessing.com/magazine/2017/april-2017/special-focus-petrochemical-developments/shaping-the-future-of-on-purpose-propylene-production (accessed 17-10-2024).

[8] Pretz M. T.; Stewart M. W. Catalytic dehydrogenation process. US 9 725 382 B2, 2014.

[9] Pretz, M.; Luo, L.; Domke, S.; Clark, H. W.; Pierce, R. A.; Malek, A. M.; Stewart, M. W.; Stears, B. A.; Schweizer, A. E., Jr.; JR. Capone, G.; Coffey, D. P.; Mbaraka, I.K. Reactivating propane dehydrogenation catalyst. US 10 065 905 B2, 2017

[10] Pretz, M. T.; Domke, S. B.; Castor W. M.; Hamper, S. J. Process for the preparation of dehydrogenated hydrocarbon compounds, EP 2 495 228 B1, 2005

[11] Iezzi, R.; Bartolini, A.; Buonomo, F. Process for preparing light olefins by dehydrogenation of the corresponding paraffins. US 7 235 706 B2, 2002

[12] Luo, L.; Rosenfeld, D. C.; Malek, A. M. Reconstituted dehydrogenation catalyst showing slowed activity loss when compared with fresh catalyst. EP 2 817 276 B1, 2013

[13] Purdy, S. C.; Seemakurthi, R. R.; Mitchell, G. M.; Davidson, M.; Lauderback, B. A.; Deshpande, S.; Wu, Z.; Wegener, E. C.; Greeley, J.; Miller, J. T. Structural Trends in the Dehydrogenation Selectivity of Palladium Alloys. *Chem. Sci.*, **2020**, *11*, 5066–5081. https://doi.org/10.1039/d0sc00875c.

[14] Baumgarten, R.; Ingale, P.; Ebert, F.; Mazheika, A.; Gioria, E.; Trapp, K.; Profita, K. D.; Naumann d'Alnoncourt, R.; Driess, M.; Rosowski, F. Controlling the Coke Formation in Dehydrogenation of Propane by Adding Nickel to Supported Gallium Oxide. *ChemCatChem*, **2023**, *16*. https://doi.org/10.1002/cctc.202301261.

[15] He, Y.; Song, Y.; Cullen, D. A.; Laursen, S. Selective and Stable Non-Noble-Metal Intermetallic Compound Catalyst for the Direct Dehydrogenation of Propane to Propylene. *J. Am. Chem. Soc.*, **2018**, *140*, 14010–14014. https://doi.org/10.1021/jacs.8b05060.

[16] Zhu, M.; Ge, Q.; Zhu, X. Catalytic Reduction of CO2 to CO via Reverse Water Gas Shift Reaction: Recent Advances in the Design of Active and Selective Supported Metal Catalysts. *Trans. Tianjin Univ.*, **2020**, *26*, 172–187. https://doi.org/10.1007/s12209-020-00246-8.

[17] Su, X.; Yang, X.; Zhao, B.; Huang, Y. Designing of Highly Selective and High-Temperature Endurable RWGS Heterogeneous Catalysts: Recent Advances and the Future Directions. *J. Energy Chem.*, **2017**, *26*, 854–867. https://doi.org/10.1016/j.jechem.2017.07.006.

[18] Kwak, J. H.; Kovarik, L.; Szanyi, J. Heterogeneous Catalysis on Atomically Dispersed Supported Metals: CO2 Reduction on Multifunctional Pd Catalysts. *ACS Catal.*, **2013**, *3*, 2094–2100. https://doi.org/10.1021/cs4001392.

[19] Wang, Z.; Wang, L.; Cui, Y.; Xing, Y.; Su, W. Research on Nickel-Based Catalysts for Carbon Dioxide Methanation Combined with Literature Measurement. *J.CO_2 Util.*, **2022**, *63*, 102117. https://doi.org/10.1016/j.jcou.2022.102117.

[20] Zhou, W.; Brack, E.; Ehinger, C.; Paterson, J.; Southouse, J.; Copéret, C. Reactivity Switch of Platinum with Gallium: From Reverse Water Gas Shift to Methanol Synthesis. *J. Am. Chem. Soc.*, **2024**, *146*, 10806–10811. https://doi.org/10.1021/jacs.4c01144

[21] Zimmerli, N. K.; Rochlitz, L.; Checchia, S.; Müller, C. R.; Copéret, C.; Abdala, P. M. Structure and Role of a Ga-Promoter in Ni-Based Catalysts for the Selective Hydrogenation of CO2 to Methanol. *JACS Au*, **2024**, *4*, 237–252. https://doi.org/10.1021/jacsau.3c00677

[22] Docherty, S. R.; Phongprueksathat, N.; Lam, E.; Noh, G.; Safonova, O. V.; Urakawa, A.; Copéret, C. Silica-Supported PdGa Nanoparticles: Metal Synergy for Highly Active and Selective CO2-to-CH3OH Hydrogenation. *JACS Au*, **2021**, *1*, 450–458. https://doi.org/10.1021/jacsau.1c00021.

[23] Siddiqi, G.; Sun, P.; Galvita, V.; Bell, A. T. Catalyst Performance of Novel Pt/Mg(Ga)(Al)O Catalysts for Alkane Dehydrogenation. *J. Catal.*, **2010**, *274*, 200–206. https://doi.org/10.1016/j.jcat.2010.06.016

[24] Sun, P.; Siddiqi, G.; Chi, M.; Bell, A. T. Synthesis and Characterization of a New Catalyst Pt/Mg(Ga)(Al)O for Alkane Dehydrogenation. *J. Catal.*, **2010**, *274*, 192–199. https://doi.org/10.1016/j.jcat.2010.06.017.

[25] Tew, M. W.; Miller, J. T.; van Bokhoven, J. A. Particle Size Effect of Hydride Formation and Surface Hydrogen Adsorption of Nanosized Palladium Catalysts: L3 Edge vs K Edge X-Ray Absorption Spectroscopy. *J. Phys. Chem. C*, **2009**, *113*, 15140–15147. https://doi.org/10.1021/jp902542f.

[26] Sumaria, V.; Nguyen, L.; Tao, F. F.; Sautet, P. Atomic-Scale Mechanism of Platinum Catalyst Restructuring under a Pressure of Reactant Gas. *J. Am. Chem. Soc.*, **2022**, *145*, 392–401. https://doi.org/10.1021/jacs.2c10179.

[27] Philippot, K.; Chaudret, B. Organometallic Approach to the Synthesis and Surface Reactivity of Noble Metal Nanoparticles. *C. R. Chimie*, **2003**, *6*, 1019–1034. https://doi.org/10.1016/j.crci.2003.07.010.

[28] Teschner, D.; Révay, Z.; Borsodi, J.; Hävecker, M.; Knop-Gericke, A.; Schlögl, R.; Milroy, D.; Jackson, S. D.; Torres, D.; Sautet, P. Understanding Palladium Hydrogenation Catalysts: When the Nature of the Reactive Molecule Controls the Nature of the Catalyst Active Phase. *Angew. Chem. Int. Ed.*, **2008**, *47*, 9274–9278. https://doi.org/10.1002/anie.200802134.

[29] Van Speybroeck, V. Challenges in Modelling Dynamic Processes in Realistic Nanostructured Materials at Operating Conditions. *Philos. Trans. R. Soc. A-Math. Phys. Eng. Sci.*, **2023**, *381*. https://doi.org/10.1098/rsta.2022.0239.

[30] Morales-García, Á.; Viñes, F.; Gomes, J. R. B.; Illas, F. Concepts, Models, and Methods in Computational Heterogeneous Catalysis Illustrated through CO_2 conversion. *Wiley Interdiscip. Rev. Comput. Mol. Sci.*, **2021**, *11*. https://doi.org/10.1002/wcms.1530.

[31] Sauer, J. The Future of Computational Catalysis. *J. Catal.*, **2024**, *433*, 115482. https://doi.org/10.1016/j.jcat.2024.115482.

[32] Cusinato, L.; del Rosal, I.; Poteau, R. Shape, Electronic Structure and Steric Effects of Organometallic Nanocatalysts: Relevant Tools to Improve the Synergy between Theory and Experiment. *Dalton Trans.*, **2017**, *46*, 378–395. https://doi.org/10.1039/c6dt04207d.

[33] Fleck, M.; Zagrovic, B. Configurational Entropy Components and Their Contribution to Biomolecular Complex Formation. *J. Chem. Theory Comput.*, **2019**, *15*, 3844–3853. https://doi.org/10.1021/acs.jctc.8b01254.

[34] Pavan, L.; Rossi, K.; Baletto, F. Metallic Nanoparticles Meet Metadynamics. *J. Chem. Phys.* **2015**, *143* (18), 184304. https://doi.org/10.1063/1.4935272.

[35] Rossi, K.; Baletto, F. The Effect of Chemical Ordering and Lattice Mismatch on Structural Transitions in Phase Segregating Nanoalloys. *Phys. Chem. Chem. Phys.* **2017**, *19* (18), 11057–11063. https://doi.org/10.1039/C7CP01397C.

[36] Piccini, G.; Lee, M.-S.; Yuk, S. F.; Zhang, D.; Collinge, G.; Kollias, L.; Nguyen, M.-T.; Glezakou, V.-A.; Rousseau, R. Ab Initio Molecular Dynamics with Enhanced Sampling in Heterogeneous Catalysis. *Catal. Sci. Technol.*, **2022**, *12*, 12–37. https://doi.org/10.1039/d1cy01329g.

[37] Rochlitz, L.; Pessemesse, Q.; Fischer, J. W. A.; Klose, D.; Clark, A. H.; Plodinec, M.; Jeschke, G.; Payard, P.-A.; Copéret, C. A Robust and Efficient Propane Dehydrogenation Catalyst from Unexpectedly Segregated Pt2Mn Nanoparticles. *J. Am. Chem. Soc.* **2022**, *144* (29), 13384–13393. https://doi.org/10.1021/jacs.2c05618.

[38] Baumgärtner, J. F.; Müller, A.; Docherty, S. R.; Comas-Vives, A.; Payard, P.-A.; Copéret, C. Metadynamics Simulations Reveal Alloying-Dealloying Processes for Bimetallic PdGa Nanoparticles under CO2 Hydrogenation. *Chem. Sci.*, **2024**, *15*, 4871–4880. https://doi.org/10.1039/d4sc00484a. https://doi.org/10.26434/chemrxiv-2023-qk5f7-v3.

[39] Payard, P.-A.; Rochlitz, L.; Searles, K.; Foppa, L.; Leuthold, B.; Safonova, O. V.; Comas-Vives, A.; Copéret, C. Dynamics and Site Isolation: Keys to High Propane Dehydrogenation Performance of Silica-Supported PtGa Nanoparticles. *JACS Au*, **2021**, *1*, 1445–1458. https://doi.org/10.1021/jacsau.1c00212.

[40] Laio, A.; Parrinello, M. Escaping Free-Energy Minima. *Proc. Natl. Acad. Sci. U.S.A.* **2002**, *99*, 12562–12566. https://doi.org/10.1073/pnas.202427399.

[41] Ciccotti, G.; Ferrario, M. Blue Moon Approach to Rare Events. *Mol. Simul.* **2004**, *30* (11–12), 787–793. https://doi.org/10.1080/0892702042000270214.

[42] Martínez, L.; Andrade, R.; Birgin, E. G.; Martínez, J. M. PACKMOL: A package for building initial configurations for molecular dynamics simulations. *J. Comput. Chem.* **2009**, *30* (13), 2157–2164. https://doi.org/10.1002/jcc.21224.

[43] Cowley, J. M. An Approximate Theory of Order in Alloys. *Phys. Rev.* **1950**, *77* (5), 669–675. https://doi.org/10.1103/PhysRev.77.669.

[44] Calvo, F.; Mottet, C. Order-Disorder Transition in Co-Pt Nanoparticles: Coexistence, Transition States, and Finite-Size Effects. *Phys. Rev. B* **2011**, *84*, 035409. https://doi.org/10.1103/PhysRevB.84.035409.

[45] Parr, R. G.; Pearson, R. G. Absolute Hardness: Companion Parameter to Absolute Electronegativity. *J. Am. Chem. Soc.* **1983**, *105* (26), 7512–7516. https://doi.org/10.1021/ja00364a005.

[46] Docherty, S. R.; Phongprueksathat, N.; Lam, E.; Noh, G.; Safonova, O. V.; Urakawa, A.; Copéret, C. Silica-Supported PdGa Nanoparticles: Metal Synergy for Highly Active and Selective CO2-to-CH3OH Hydrogenation. *JACS Au*, **2021**, *1*, 450–458. https://doi.org/10.1021/jacsau.1c00021.

[47] McCue, A. J.; Anderson, J. A. CO Induced Surface Segregation as a Means of Improving Surface Composition and Enhancing Performance of CuPd Bimetallic Catalysts. *J. Catal.* **2015**, *329*, 538–546. https://doi.org/10.1016/j.jcat.2015.06.002.

[48] Wang, W. J.; Hwang, S.; Kim, T.; Ha, S.; Scudiero, L. Study of Carbon Supported CuPd Alloy Nanoparticles with Pd-Rich Surface for the Electrochemical Formate Oxidation and CO2 Reduction. *Electrochimica Acta* **2021**, *387*, 138531. https://doi.org/10.1016/j.electacta.2021.138531.

[49] Payard, P.-A.; Rochlitz, L.; Searles, K.; Foppa, L.; Leuthold, B.; Safonova, O. V.; Comas-Vives, A.; Copéret, C. Dynamics and Site Isolation: Keys to High Propane Dehydrogenation Performance of Silica-Supported PtGa Nanoparticles. *JACS Au*, **2021**, *1*, 1445–1458. https://doi.org/10.1021/jacsau.1c00212

[50] Yadav, M.; Szenti, I.; Ábel, M.; Szamosvölgyi, Á.; Ábrahámné, K. B.; Kiss, J.; Zsolt, P.; Sápi, A.; Kukovecz, Á.; Kónya, Z. Concentrated Platinum-Gallium Nanoalloy for Hydrogen Production from the Catalytic Steam Reforming of Ethanol. *ChemCatChem*, **2022**, *15*. https://doi.org/10.1002/cctc.202200717.

[51] Alharis, R. A.; McMullin, C. L.; Davies, D. L.; Singh, K.; Macgregor, S. A. Understanding Electronic Effects on Carboxylate-Assisted C–H Activation at Ruthenium: The Importance of Kinetic and Thermodynamic Control. *Faraday Discuss.*, **2019**, *220*, 386–403. https://doi.org/10.1039/c9fd00063a.

[52] Chaudret, B. Synthesis and Surface Reactivity of Organometallic Nanoparticles. *Top. Organomet. Chem.*, 233–259. https://doi.org/10.1007/b138079.